Journal of Solid State Chemistry 181 (2008) 1998–2005

Contents lists available at ScienceDirect

Journal of Solid State Chemistry

journal homepage: www.elsevier.com/locate/jssc

Electron charge distribution of $CaAl_{2-x}Zn_x$: Maximum entropy method combined with Rietveld analysis of high-resolution-synchrotron X-ray powder diffraction data

Karin Söderberg [a], Yoshiki Kubota [b], Norihiro Muroyama [a], Daniel Grüner [a], Arisa Yoshimura [b], Osamu Terasaki [a,*]

[a] Arrhenius Laboratory, Department of Physical, Inorganic and Structural Chemistry, Stockholm University, Stockholm 10691, Sweden
[b] Graduate School of Science, Department of Physical Science, Osaka Prefecture University, Sakai, Osaka 599-8531, Japan

ARTICLE INFO

Article history:
Received 19 December 2007
Received in revised form
11 April 2008
Accepted 24 April 2008
Available online 8 May 2008

Keywords:
Intermetallic compounds
Laves phases
Charge density
Maximum entropy method

ABSTRACT

Using short wavelength X-rays from synchrotron radiation (SPring-8), high-resolution powder diffraction patterns were collected. In order to study both the structural relationship and the mechanism of stability in the $CaAl_{2-x}Zn_x$ system, among the Laves phases ($MgCu_2$ and $MgNi_2$ type) and KHg_2-type structures, the charge density distribution of $CaAl_{2-x}Zn_x$ as a function of x was obtained from the diffraction data by Rietveld analysis combined with the maximum entropy method (MEM). In the MEM charge density maps overlapping electron densities were clearly observed, especially in the Kagomé nets of the Laves phases. In order to clarify the charge redistribution in the system, the deformation charge densities from the densities formed by the constituent free atoms are discussed. In the ternary $MgNi_2$-type phase, partial ordering of Al and Zn atoms is observed, a finding that is supported by ab-initio total energy calculations.

1. Introduction

Extensive work has been reported on the Laves phases describing their crystal structures, phase stability, and various metallurgical properties after the pioneering works [1–4]. These phases have a composition AB_2 where the A atom is larger than the B atom. The Laves phases belong to the class of Frank–Kasper phases, i.e., topologically closed packed structures with different atomic sizes. The larger A atoms are in the center of a Frank–Kasper polyhedron with coordination number 16 ($4A$ and $12B$ atoms) and the smaller B atoms are at the center of an icosahedron with coordination number 12 ($6A$ and $6B$ atoms) [5]. The ideal atomic radius ratio, calculated from the packing of hard spheres of A and B atoms, is $r_A/r_B = \sqrt{3/2} \approx 1.225$.

Three primary structure types of Laves phases have been reported: cubic C15 (3C)-$MgCu_2$ type ($Fd\bar{3}m$), hexagonal C14 (2H)-$MgZn_2$ type ($P6_3/mmc$) and hexagonal C36 (4H)-$MgNi_2$ type ($P6_3/mmc$). Figs. 1(a)–(c) show schematic drawings of C15-, C36- and C14-type structures, respectively, in projection along the a axis, where the cubic C15 structure is shown in the hexagonal setting. The crystal structures can be described by two interpenetrating nets of A and B atoms. The A atoms form a cubic diamond net in the C15 structure, a hexagonal diamond net in the C14 structure, and a periodic intergrowth of the cubic and the hexagonal diamond networks in the C36 structure (as observed in 4H-SiC). The smaller B atoms form a three-dimensional six-connected net of all-vertex-connected tetrahedra in the C15 structure, whereas tetrahedra are alternately vertex- and face-sharing in the C14 structure. The B atom network in the C36 structure can again be described as a periodic intergrowth of the structural motif observed in the C15 and C14 structures. Another way to describe the B atom network in the crystal structures of the Laves phases is a stacking of Kagomé (3.6.3.6) nets along the cubic $\langle 111 \rangle$ or the hexagonal [001] directions. The triangles of the Kagomé net are capped by B atoms. In the C15 structure, each triangle is capped by one B atom, where the capping atoms of neighboring triangles lie on opposite sides of the Kagomé net plane. In the C14 structure, every second triangle is capped above and below the net plane, whereas the remaining triangles are uncapped. The C36 structure contains two types of Kagomé nets, one with the capping pattern of the C15 type, the other with that of the C14 type. In each structure, the capping atoms are shared between two Kagomé nets, thereby building up the three-dimensional B network. The B network of the C36 structure and the capping patterns of the Kagomé nets are shown in Fig. 2.

In many intermetallic systems, the KHg_2-type structure has been observed as a neighboring phase to the Laves phases in terms of atomic size ratio, that is, for a larger ratio of r_A/r_B than the

* Corresponding author. Fax: +46 8 152187.
E-mail address: terasaki@struc.su.se (O. Terasaki).

0022-4596/$ - see front matter © 2008 Elsevier Inc. All rights reserved.
doi:10.1016/j.jssc.2008.04.034

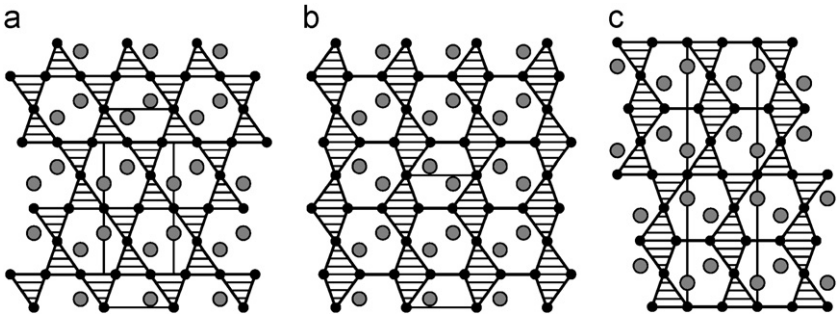

Fig. 1. Schematic drawings of the crystal structures of C15 (a), C14 (b), and C36 type (c) viewed along the *a*-axis. The *B* net is shown by hatched tetrahedra and *A* atoms are represented by gray spheres. Unit cell edges are also shown (rhombohedral cell with hexagonal axes for C15).

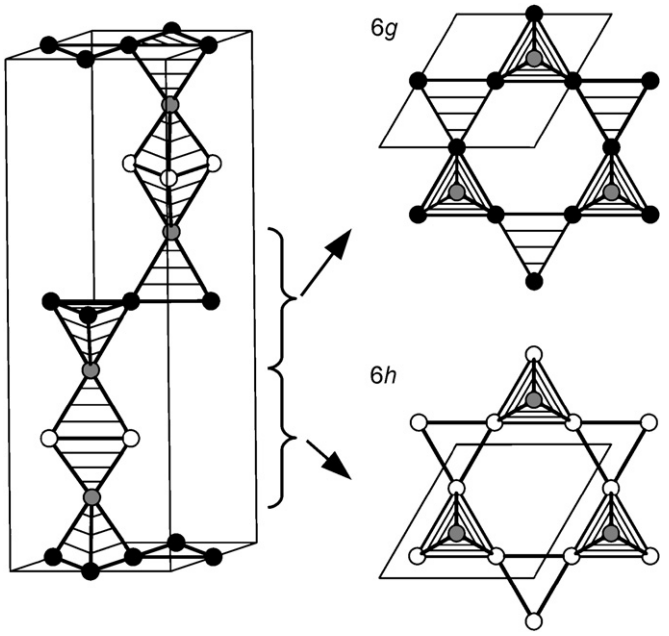

Fig. 2. The *B* network of the C36 structure. Grey, black, and white circles represent atoms on the Wyckoff positions 4*f*, 6*g*, and 6*h*, respectively. On the right-hand side of the figure, projections of the capped Kagomé nets onto the *ab* plane are shown.

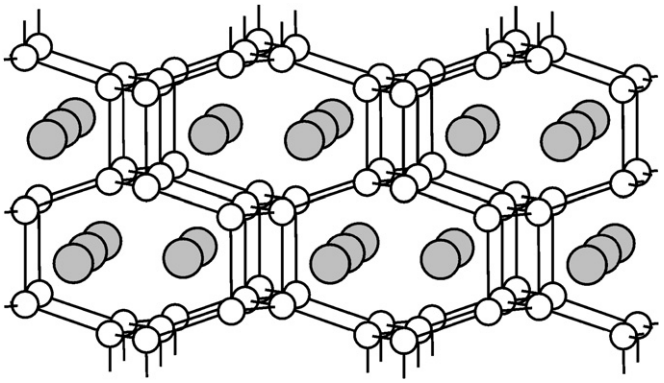

Fig. 3. The crystal structure of $CaZn_2$ (KHg_2 type) viewed approximately along the *a*-axis. Ca and Zn atoms are drawn as gray and white spheres, respectively.

Laves phase. The KHg_2-type structure comprises a three-dimensional four-connected net of the smaller *B* atoms. This net can be constructed by stacking layers of condensed six-membered rings as observed in black phosphorous with an *AB* stacking sequence [6]. This stacking creates channels running along [100], which are filled with zigzag chains of the larger *A* atoms. The crystal structure of $CaZn_2$ crystallizing with KHg_2-type structure is shown in Fig. 3.

In our previous study on the phase stabilities in the $CaAl_{2-x}Zn_x$ system, we have found a new hexagonal C36-type Laves structure in the composition range of $0.3 \leqslant x \leqslant 0.65$ surrounded by C15-type ($0 \leqslant x \leqslant 0.15$) and KHg_2-type ($0.95 \leqslant x \leqslant 2$) phases [7].

For the Laves phases, it has been pointed out from an early stage that two factors, the atomic size radius ratio of *A*–*B* atoms and the electron atom ratio (*e*/*a*) or valence electron concentration (VEC), play an important role in structure stabilization. From single crystal X-ray diffraction measurements, Ohba et al. obtained crystal structure factors for $MgNi_2$ (C14 type) and $MgCu_2$ (C15 type), and found (i) the Kagomé net is not deformed in $MgCu_2$ but is deformed in $MgNi_2$, (ii) electron transfer from Mg to Ni in $MgNi_2$ and from Cu to Mg in $MgCu_2$ crystals, respectively [8]. Kubota et al. also studied electron charge density distributions in Mg-based Laves phase systems, $MgCu_2$ and $MgZn_2$, from synchrotron powder diffraction data by the maximum entropy method (MEM). They found overlapping electron density in the Kagomé net between Cu atoms in $MgCu_2$ and between Zn atoms in $MgZn_2$ while no overlapping electron density between Mg and Cu or Mg and Zn was observed. It was claimed that the Kagomé net was an electronic network, which helps to stabilize the structures rather than a geometrical concept [9,10]. In a theoretical study of the valence charge density in simple metal Laves phases, increased charge density in the center of tetrahedra formed by the small atoms is attributed to chemical bonding effects [11].

In this report, we study the electron density distribution and its composition dependence in the pseudo-binary $CaAl_{2-x}Zn_x$ system. The electron density distributions of $CaAl_{2-x}Zn_x$ were obtained as a function of composition *x* from the Rietveld/MEM analysis of synchrotron powder X-ray diffraction data collected with short wavelength and high resolution in order to obtain accurate intensity data for as many reflections as possible.

2. Experimental

2.1. Sample preparation

Polycrystalline samples of $CaAl_{2-x}Zn_x$ with $x = 0$, 0.1, 0.3, 0.5, 0.65, and 2.0 were synthesized. The average weight of a sample for one experiment was 0.5 g. Starting materials were calcium (crystalline dendritic pieces, Alfa Aesar, 99.987%), zinc (shots, Alfa Aesar, 99.9999%) and aluminum (rods, Alfa Aesar, 99.9965%). Calcium pieces, zinc shots and pieces of the aluminum rod were weighed in the respective atomic ratios and placed in sealed tantalum tubes under an argon atmosphere. The Ta tubes were jacketed in sealed quartz tubes and homogenized at 1273 K

($x \geqslant 1.0$) or at 1373 K ($x < 1.0$) for 2 h. Finally the Ta tube with the products were annealed at 873 K for 21 days ($x \geqslant 1.1$) or at 973 K for 11 days ($x < 1.1$) and then quenched to room temperature by plunging the samples into water. The silvery gray samples could be easily separated from the tantalum tubes. No visible reactions of the samples with the crucible material could be detected. From the TEM observations, it was confirmed that all the samples were uniform in composition and there were no stacking defects or intergrowths [12]. Fine powders with uniform particle size were prepared by first crushing the ingot and then using the precipitation method inside a glove box, and sealed in 0.3 mm diameter glass capillaries. The granularity of the powders was confirmed by a homogeneous intensity distribution in the Debye–Scherrer powder ring and also by standard electron microscopy (SEM) images, which show small and uniform sized particles with an average size of 10 μm.

2.2. Synchrotron X-ray powder diffraction

High-resolution X-ray powder diffraction patterns were collected with the Debye–Scherrer camera at the beam line BL02B2, SPring-8, Japan. A monochromatic incident X-ray beam was obtained using a (111) Si double-crystal monochromator, and the wavelength was determined to be $\lambda = 0.401(3)$ Å. Using an imaging plate (IP) as a detector, it was possible to collect a whole powder pattern simultaneously with very high dynamic range and high accuracy (both in spatial resolution and intensity) at reasonable experimental time under the same experimental conditions. The pixel size of the IP is $50 \times 50\,\mu m^2$ and the radius of the camera is 286.5 mm, which leads to a resolution of 0.01° in 2θ scattering angle. The size of the IP is $200 \times 400\,mm^2$, which covers up to 80.0° in 2θ. Samples were cooled to 200 K using a N_2 gas flow and rotated during measurement. Cooling to lower temperatures was impeded by the crystallization of significant amounts of ice on the capillaries. Even at 200 K, very weak diffraction lines from ice were sometimes observed; however, these were recognized easily as spotty rings in the original IP data and not included in Rietveld analysis.

The electron charge distributions were obtained by combination of the MEM and the Rietveld refinement. The procedure of the MEM/Rietveld analysis has been described in detail previously [13,14]. The background (mainly from the glass capillaries) was modeled using a combination of split Pearson VII functions, whereas the reflection profiles were described by individual split Pearson VII functions. Atomic form factors of the neutral atoms, which were corrected for anomalous dispersion, were used [15]. The Rietveld refinements were carried out using the program rwpy917 [16]. Reflections up to 1.22 $Å^{-1}$ in $\sin\theta/\lambda$ for C15-type, 1.09 $Å^{-1}$ for C36-type, and 0.92 $Å^{-1}$ for KHg_2 type were used for the Rietveld refinement. MEM analysis was carried out with $64 \times 64 \times 64$ and $32 \times 32 \times 128$ pixels per unit cell for C15 and C36 type, respectively, using the computer program ENIGMA [17].

In order to emphasize overlapping electron densities between the atoms, deformation charge densities $\Delta\rho(\boldsymbol{r})$ were calculated from observed structure factors, $F_{obs}(g_{h\,k\,l})$, and calculated ones, $F_{cal}(\boldsymbol{g}_{h\,k\,l})$, in the Rietveld analysis in the above mentioned range of $\sin\theta/\lambda$. The $F_{cal}(\boldsymbol{g}_{h\,k\,l})$ are calculated using the atomic scattering factors for free Ca, Al, and Zn atoms in their analytical form of $\sum_{i=1,4} a_i \exp(-b_i s^2) + c$ together with atomic coordinates and occupation probabilities obtained by the Rietveld analysis in order to keep internal consistency. $\Delta\rho(\boldsymbol{r})$ is then given an approximate value by the following Fourier difference map:

$$\Delta\rho(\boldsymbol{r}) \approx \sum_{\boldsymbol{g}_{h\,k\,l}} [F_{obs}(\boldsymbol{g}_{h\,k\,l}) - F_{cal}(\boldsymbol{g}_{h\,k\,l})] \exp 2\pi i \boldsymbol{g}_{h\,k\,l} \cdot \boldsymbol{r}.$$

For all compounds investigated in this study, small deformation charges are left in atomic core regions due to artifacts in the Fourier difference map. Therefore, we will not discuss deformation densities in the core regions in this paper. As mentioned above, the main purpose of the deformation density maps is to emphasize the electron density in the interatomic region, which is already visible in the MEM electron density maps.

2.3. Computational methods

Electronic structure calculations within the local density approximation (LDA) to the density functional theory were carried out using VASP [18] and Vanderbilt-type ultrasoft pseudopotentials [19]. The Perdew–Zunger parameterization of the exchange-correlation functional was used [20]. The cut-off energy was set to 240 eV. All calculations were carefully checked for convergence, and total energies are converged to 0.1 meV per atom. After relaxations, forces acting on the atoms are less than 0.05 eV/Å.

3. Results and discussion

All diffraction lines of the samples were sharp except those of $CaZn_2$. Furthermore, the sample containing $CaZn_2$ as a majority phase also contained small amounts of Zn metal which was included in the Rietveld refinements. In the later stage of the refinement, however, all parameters describing the Zn phase were kept fixed. The crystal data and structural parameters refined by the Rietveld analysis of the powder diffraction data are summarized in Tables 1 and 2 together with the reliability factor based on the Bragg intensities, R_I, and the weighted profile factor, R_{wp}. Judging from their reliability and goodness-of-fit (GoF) factors, the Rietveld refinements were carried out successfully although the refinement for $CaZn_2$ is not as good as of the other materials. Therefore, we do not include a MEM analysis for $CaZn_2$.

Observed and calculated diffraction patterns of C36 $CaAl_{1.35}Zn_{0.65}$ are shown in Fig. 4. The magnitudes of the observed crystal structure factors, $|F_{obs}(hkl)|$, were extracted from the powder diffraction data. The phases of the crystal structure factors $F_{obs}(hkl)$ are calculated based on the space groups, which were confirmed by transmission electron microscopy (TEM) observations including convergent beam electron diffraction patterns [12].

3.1. Crystal chemistry

Before discussing the MEM charge density, the crystal structures of the investigated compounds will be discussed. Two important aspects of the C36 structures have already been briefly mentioned in our previous paper [7]:

(i) Deviations of the atomic positions in the Kagomé net formed by atoms on the 6*h* site (site symmetry *mm*2) from the ideal position $x(6h) = 1/6 \approx 0.1666$ corresponding to a uniform Kagomé net are clearly observed. This distortion is not dependent on the composition.
(ii) A tendency for preferential occupation of the 6*h* site by Zn becomes less prominent as *x* increases, as shown in Fig. 5. Here, we will analyze these results in more detail.

Distortions of the flexible Kagomé net formed by atoms on the 6*h* position have been frequently observed for hexagonal Laves phases and analyzed in detail by electronic structure calculations [21]. In most cases, the distortion leads to an elongation of the

Table 1
Crystallographic data and details of the Rietveld refinements and MEM analyses of $CaAl_{2-x}Zn_x$ ($x = 0$, 0.1, 0.3, 0.5, 0.65, and 2)

Chem. Formula	$CaAl_2$	$CaAl_{1.9}Zn_{0.1}$	$CaAl_{1.7}Zn_{0.3}$ [7]	$CaAl_{1.5}Zn_{0.5}$	$CaAl_{1.35}Zn_{0.65}$	$CaZn_2$
Space group, Z	$Fd\bar{3}m$ (origin choice 2), 8	$Fd\bar{3}m$ (origin choice 2), 8	$P6_3/mmc$, 8	$P6_3/mmc$, 8	$P6_3/mmc$, 8	$Imma$, 4
a/Å	8.04144(1)	8.02017(3)	5.68894(2)	5.67986(1)	5.66603(2)	4.5850(1)
b/Å						7.3662(2)
c/Å			18.3384(1)	18.32396(8)	18.30293(9)	7.6653(2)
V/Å^3	519.998(2)	515.882(4)	513.990(7)	511.947(5)	508.873(7)	258.89(2)
No. of profile points/no. of reflections	7178/341	6006/233	6031/1830	6086/1856	5784/1631	4854/746
R_{wp}	0.040	0.011	0.016	0.028	0.018	0.025
R_I	0.021	0.011	0.020	0.015	0.015	0.021
GoF	2.00	1.40	1.93	2.48	1.76	4.92
No. of reflections used for MEM	226	229	1718	1792	1623	
R_{MEM}	0.012	0.012	0.020	0.021	0.019	

Further details of the crystal structure investigations can be obtained from the Fachinformationszentrum Karlsruhe, 76344 Eggenstein-Leopoldshafen, Germany (fax: +49 7247 808 666; e-mail: crysdata@fiz-karlsruhe.de) on quoting the depository numbers CSD-418966 ($CaAl_2$), CSD-418967 ($CaAl_{1.9}Zn_{0.1}$), CSD-418968 ($CaAl_{1.7}Zn_{0.3}$), CSD-418969 ($CaAl_{1.5}Zn_{0.5}$), CSD-418970 ($CaAl_{1.35}Zn_{0.65}$), and CSD-418971 ($CaZn_2$).

Table 2
Site occupancies, atomic coordinates, and isotropic thermal parameters (Å^2) for $CaAl_{2-x}Zn_x$ ($x = 0$, 0.1, 0.3, 0.5, 0.65, 2)

Atom	Site	g	x	y	z	B
$CaAl_2$						
Al	16*c*	1.0	0	0	0	0.537(6)
Ca	8*b*	1.0	3/8	3/8	3/8	0.464(4)
$CaAl_{1.9}Zn_{0.1}$						
Al	16*c*	0.953(1)	0	0	0	0.598(8)
Zn		0.047				
Ca	8*b*	1.0	3/8	3/8	3/8	0.526(6)
$CaAl_{1.7}Zn_{0.3}$ [7]						
Al	6*h*	0.8068(7)	0.1624(2)	2*x*	1/4	0.636(6)
Zn		0.1932				
Al	6*g*	0.8855(7)	1/2	0	0	
Zn		0.1145				
Al	4*f*	0.8617(9)	1/3	2/3	0.12922(4)	
Zn		0.1383				
Ca	4*f*	1.0	1/3	2/3	0.65573(4)	0.502(5)
Ca	4*e*	1.0	0	0	0.09312(4)	
$CaAl_{1.5}Zn_{0.5}$						
Al	6*h*	0.6864(8)	0.1621(2)	2*x*	1/4	0.620(7)
Zn		0.3136				
Al	6*g*	0.7821(8)	1/2	0	0	
Zn		0.2179				
Al	4*f*	0.797(1)	1/3	2/3	0.12969(5)	
Zn		0.203				
Ca	4*f*	1.0	1/3	2/3	0.65605(5)	0.486(8)
Ca	4*e*	1.0	0	0	0.09297(4)	
$CaAl_{1.35}Zn_{0.65}$						
Al	6*h*	0.6088(7)	0.1625(1)	2*x*	1/4	0.645(5)
Zn		0.3912				
Al	6*g*	0.6982(7)	1/2	0	0	
Zn		0.3018				
Al	4*f*	0.7396(9)	1/3	2/3	0.12983(4)	
Zn		0.2604				
Ca	4*f*	1.0	1/3	2/3	0.65579(4)	0.444(5)
Ca	4*e*	1.0	0	0	0.09314(4)	
$CaZn_2$						
Zn	8*h*	1.0	0	0.05892(6)	0.16447(7)	0.669(7)
Ca	4*e*	1.0	0	1/4	0.5478(2)	0.39(2)

edges of the doubly capped triangles in the Kagomé net, while the edges of the uncapped triangles are shortened. Although the distortion is present even for Laves phases of ideal composition AB_2, e.g., $MgZn_2$, its magnitude may be influenced by substitutional disorder. In the present case, however, no significant change of the distortion with the composition is observed. A similar behavior was observed for C36 $CaAl_{2-x}Mg_x$, where the distortion does not change significantly with Mg content ($x(6h) = 0.1629$ and $x(6h) = 0.1634$ for $x = 0.66$ and 1.34, respectively) [22].

In order to further check the influence of substituting Al by Zn, the distortions observed in the ternary C36 phase $CaAl_{2-x}Zn_x$ may be compared with the distortions of the hypothetical binary C36 phases $CaAl_2$ and $CaZn_2$ with optimized structural parameters (c/a ratio, atomic coordinates). In the case of the Ca–Al system, the total energy of the C36 structure is 12 meV per formula unit $CaAl_2$ (1.2 kJ/mol) higher than that of the stable C15 structure, whereas in the Ca–Zn system, the total energy difference between the C36 structure and the stable KHg_2-type structure is 45 meV per formula unit $CaZn_2$ (4.3 kJ/mol).

For the hypothetical binary C36 $CaAl_2$, a very similar distortion ($x(6h) = 0.1624$) as observed in ternary C36 $CaAl_{2-x}Zn_x$ is predicted. On the other hand, for hypothetical C36 $CaZn_2$, the predicted distortion is smaller than that of C36 $CaAl_2$ ($x(6h) = 0.1650$). Please note that, at the Zn-rich border of the homogeneity range of C36 $CaAl_{2-x}Zn_x$, less than 1/3 of the Al atoms are replaced by Zn. It can therefore be concluded that the substitution of Al by Zn does not change structural distortions with respect to hypothetical binary C36 $CaAl_2$ significantly although a slightly decreasing distortion could be expected considering the distortions predicted for the binary C36 phases.

The site preference observed for C36 $CaAl_{2-x}Zn_x$ can also be compared with that observed for $CaAl_{2-x}Mg_x$ [22]. For $CaAl_{2-x}Zn_x$, Zn atoms prefer the 6*h* sites throughout the homogeneity range of the C36 phase, whereas for $CaAl_{2-x}Mg_x$ ($x = 0.66$), these sites are preferred by Al atoms. Zn has a smaller metal atom radius and larger electronegativity than Al, whereas Mg has a larger radius and smaller electronegativity than Al. It is thus a common pattern to $CaAl_{2-x}Zn_x$ and $CaAl_{2-x}Mg_x$ that the 6*h* site, i.e., the flexible Kagomé net, is preferentially occupied by the maller, more electronegative atom.

In order to study the site preference of Zn for the 6*h* site, the total energies of different model structures were studied. In these models, 2, 4, or 5 of the 16 Al atoms in the unit cell of C36 $CaAl_2$ are replaced by Zn atoms in an ordered manner. These compositions correspond to $CaAl_{2-x}Zn_x$ with $x = 0.25$, 0.5, and 0.625, respectively, i.e., compositions close to those of the samples investigated by the Rietveld method ($x = 0.3$, 0.5, and 0.65).

For the convenience of the reader the site occupancies determined by the Rietveld refinements are given in terms of the average total number of Zn atoms on the 4*f*, 6*g*, and 6*h* sites in Table 3. This allows for an easy comparison with the model structures used in the calculations. Whereas for $x = 0.3$, it is difficult to describe the substitution pattern by a single model

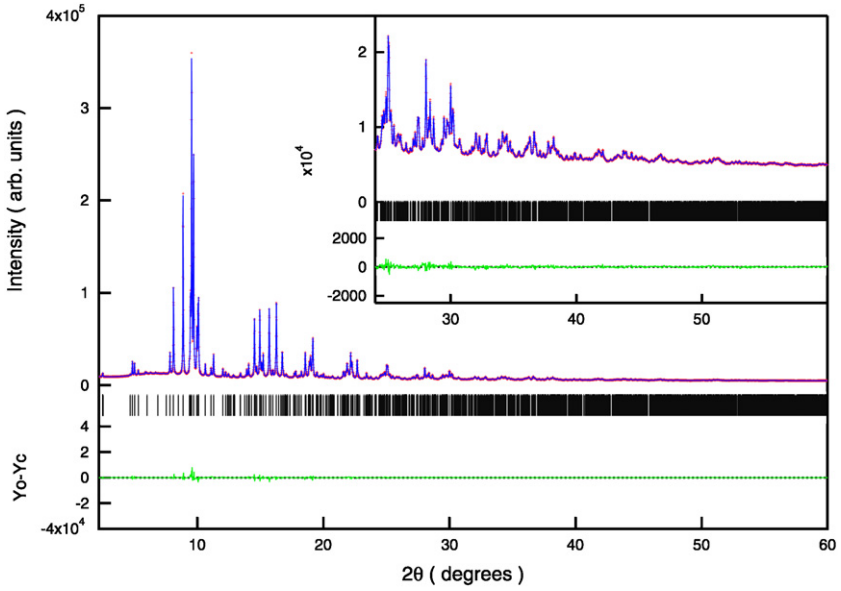

Fig. 4. Observed (red) and calculated (blue) X-ray powder diffraction patterns of $CaAl_{1.35}Zn_{0.65}$. Reflection positions are indicated by tic marks. The inset shows a magnified view of the region $2\theta > 22^\circ$. A difference curve (observed minus calculated intensity) is shown at the bottom.

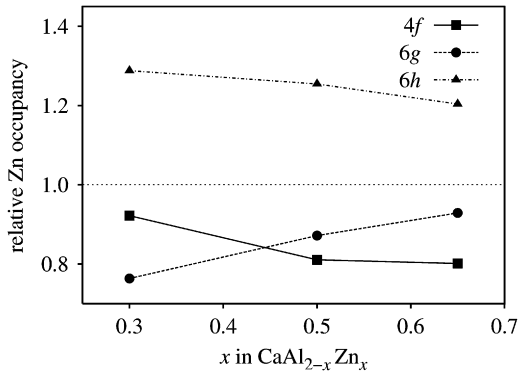

Fig. 5. Relative Zn occupancy in C36 $CaAl_{2-x}Zn_x$ as function of x.

structure, in case of $x = 0.5$ and 0.65, the experimentally observed distribution of Zn atoms is well described by the 1/1/2 (Zn(4*f*)/Zn(6*g*)/Zn(6*h*)) and 1/2/2 model structures, respectively. For each composition, a number of models with different distributions of Zn/Al atoms among the *B* sites have been investigated. The results are summarized in Table 4.

If 2 out of 16 Al atoms are replaced with Zn, a model with both Zn atoms on 6*h* position (A6 in Table 4) is energetically favoured, but a model structure with Zn atoms on 4*f* and 6*h* (A2) has only a slightly larger total energy, followed by a model with both Zn atoms on the 4*f* position (A4). Higher energies are observed for models containing Zn on the 6*g* position, the highest energy being associated with a model containing 2 Zn atoms on this position (A5). Three models with 4 Al atoms replaced with Zn have been investigated. Model B3, the Zn atom distribution of which is close to the experimentally observed average numbers on the three crystallographic sites of the *B* network, turns out to be energetically most favorable, whereas in the least stable configuration (*B*2), Zn atoms accumulate on the 6*g* position. The slight preference of the 6*g* site over the 4*f* site cannot be captured by the models. The situation is less clear for the highest degree of substitution studied here, where 5 Al atoms are replaced with Zn. Both models with 2 Zn atoms on the 6*h* position (C1 and C2) have the same total energy which is slightly lower than that of a model containing only 1 Zn atom on the 6*h* site (C3).

The effect of forming Zn–Zn contacts in the *B* network can also be studied by total energy calculations. In model A6, 2 Zn atoms are placed on two different flexible Kagomé nets (at $z = 0.25$ and 0.75). Placing the 2 Zn atoms on the same (e.g., $z = 0.25$) Kagomé net creates one Zn–Zn contact. This configuration has almost the same energy as the model with distant Zn atoms. On the other hand, considerable energy differences occur when the number of

Table 3
Average number of Zn atoms in the *B* network of C36 $CaAl_{2-x}Zn_x$

X	Zn (4*f*)	Zn (6*g*)	Zn (6*h*)
0.30	0.553(4)	0.687(3)	1.159(3)
0.50	0.810(4)	1.307(4)	1.882(4)
0.65	1.052(4)	1.811(3)	2.337(3)

Table 4
Total energies of ordered C36 $CaAl_{2-x}Zn_x$ models ($x = 0.25$, 0.5, and 0.625)

Model no.	No. of Zn atoms on position			Total energy/eV/unit cell
	4*f*	6*g*	6*h*	
$Ca_8Al_{14}Zn_2$				
A1	0	1	1	0.056
A2	1	0	1	0.015
A3	1	1	0	0.067
A4	2	0	0	0.026
A5	0	2	0	0.099
A6	0	0	2	0
$Ca_8Al_{12}Zn_4$				
B1	2	1	1	0.031
B2	1	2	1	0.048
B3	1	1	2	0
$Ca_8Al_{11}Zn_5$				
C1	1	2	2	0
C2	2	1	2	0.001
C3	2	2	1	0.014

For each composition, the energy of the lowest-energy structure defines the zero of the energy scale.

Zn–Zn contacts between flexible Kagomé nets and capping atoms are changed. Reducing the number of these contacts by placing two Zn atoms on the same Kagomé net, away from a capping Zn atom, increases stability, e.g., by 21 meV/unit cell for model B3 (in Table 4, only the energies of the most stable model structures are listed). In case of the rigid Kagomé net, this effect is much smaller, e.g., 5 meV/unit cell for model B2. The order of total energies, however, is unchanged.

Generally speaking, the energy differences between the different model structures are fairly small, i.e., less than 5 meV per atom. Complete ordering of Al/Zn atoms can thus not be expected, and it is not observed in the experiments. However, the calculations on simple model structures qualitatively confirm the experimentally observed preference of Zn for the 6*h* site.

3.2. MEM charge density

The MEM charge density and deformation charge density maps of C15 $CaAl_2$ are shown exemplary in Fig. 6, left- and right-hand side, respectively. Ca atoms, the larger atoms in the MEM maps, occupy the 8*b* sites (point group (PG) symmetry $\bar{4}3m$), and Al/Zn atoms the 16*c* sites (PG symmetry $\bar{3}m$). The electron distribution around Ca atoms deviates slightly from a spherical distribution showing a rounded triangular shape, which is commensurate with the PG symmetry. No significant overlap of the electron densities between Ca and Al/Zn atoms is observed. The overlap of electron densities between Al/Zn atoms in the (110) plane (Fig. 6a) is not clear in $CaAl_2$ but clearly observed in $CaAl_{1.9}Zn_{0.1}$. In order to obtain information of the distribution of the valence electron density, the deformation charge distributions are shown on the right-hand side in Fig. 6. For $CaAl_2$, only weak maxima are observed near the Al atoms in the (110) plane. No maxima are observed on the Al–Al contacts. In the case of $CaAl_{1.9}Zn_{0.1}$, maxima on lines connecting Al/Zn atoms are clearly observed. Additional, but weaker, maxima are found on Ca–Ca contacts. The MEM charge density and deformation charge density maps of the (111) plane containing a Kagomé net are shown in Fig. 6(b). The electron densities overlap in the Kagomé net both in $CaAl_2$ and $CaAl_{1.9}Zn_{0.1}$. In the case of $CaAl_2$, a ring-shaped region of slightly positive deformation density is found in the triangles of the Kagomé net. In $CaAl_{1.9}Zn_{0.1}$ overlapping electron density along the lines connecting Al/Zn atoms leads to clear maxima in the deformation charge density map. Additional maxima are observed in the centers of the hexagons in the Kagomé net, corresponding to the midpoints of the Ca–Ca contacts.

For a C36-type Laves phase, represented by $CaAl_{1.35}Zn_{0.65}$, the MEM charge density and deformation charge density maps of the

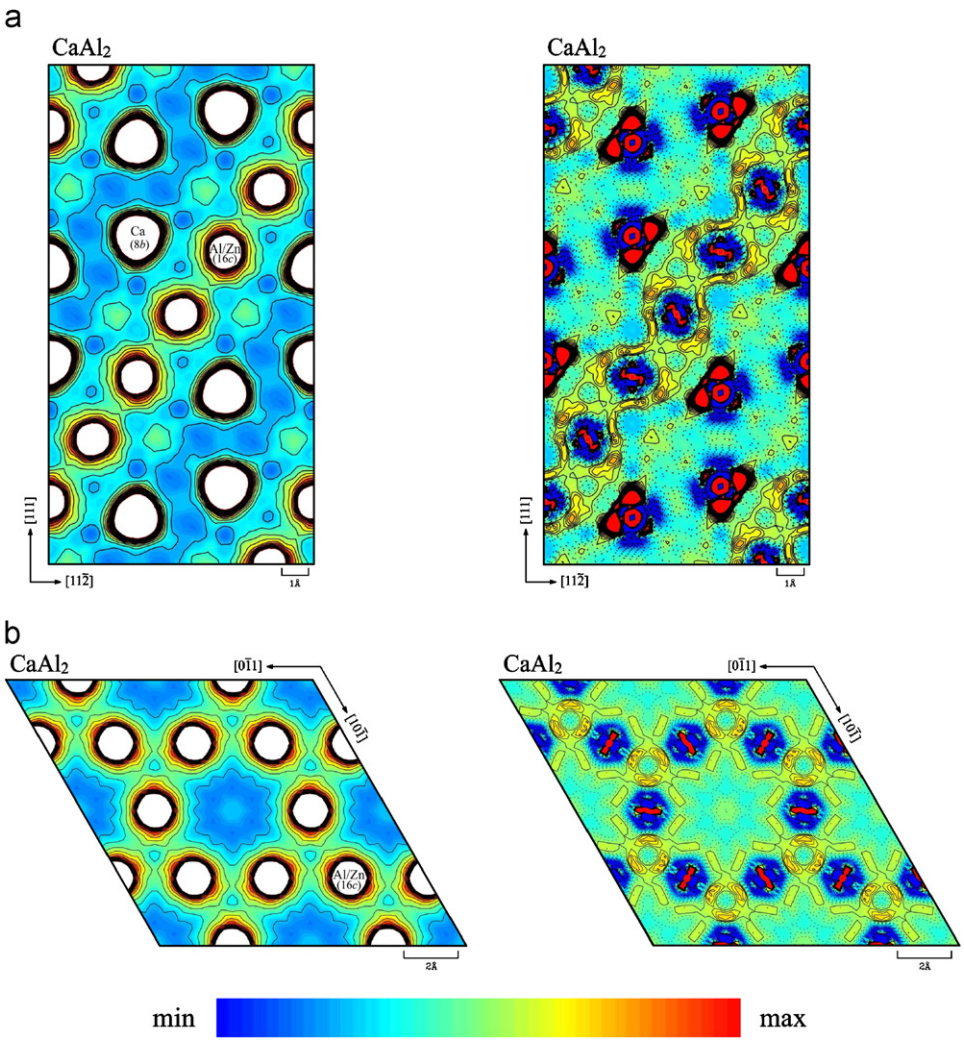

Fig. 6. The MEM charge (left) and the deformation charge (right) density maps of cubic $CaAl_2$ corresponding to the (110) section (a) and the Kagomé net in the (111) plane (b). The color code corresponds to a range (i) from 0.0 to 1.0 with a step of 0.05 e/Å^3 for the MEM map and (ii) from −0.2 to 0.2 with a step of 0.01 eÅ^{-3} for the deformation map.

(110) section and the (001) sections at $z = 0$ and $\frac{1}{4}$ (the Kagomé net planes) are shown in Figs. 7(a)–(c), respectively.

The charge distribution around the Ca atoms is nearly spherical and the overlap of the electron densities between Ca atoms and *B* net atoms is very weak. On the other hand, overlap of the densities between *B* atoms in the Kagomé net are clearly observed at both $z = 0$ and $\frac{1}{4}$ sections. Less pronounced overlap is observed between the Kagomé net atoms and the capping Al/Zn atoms occupying the 4*f* position. The electron density distribution in the Kagomé nets formed by Al/Zn atoms on the positions 6*g* and 6*h* is significantly different. Furthermore, the two different triangles (capped/uncapped) in the 6*h* Kagomé can be clearly distinguished on the basis of the electron density distribution. In all three C36 samples, the larger deformation density can be associated with the doubly capped triangle. For the uncapped triangles, the deformation density in the center is higher than that along the edges, whereas the density distribution in the capped triangles changes with composition. Following composition-dependent details of the MEM charge density are observed for $CaAl_{1.7}Zn_{0.3}$, $CaAl_{1.5}Zn_{0.5}$ and $CaAl_{1.35}Zn_{0.65}$.

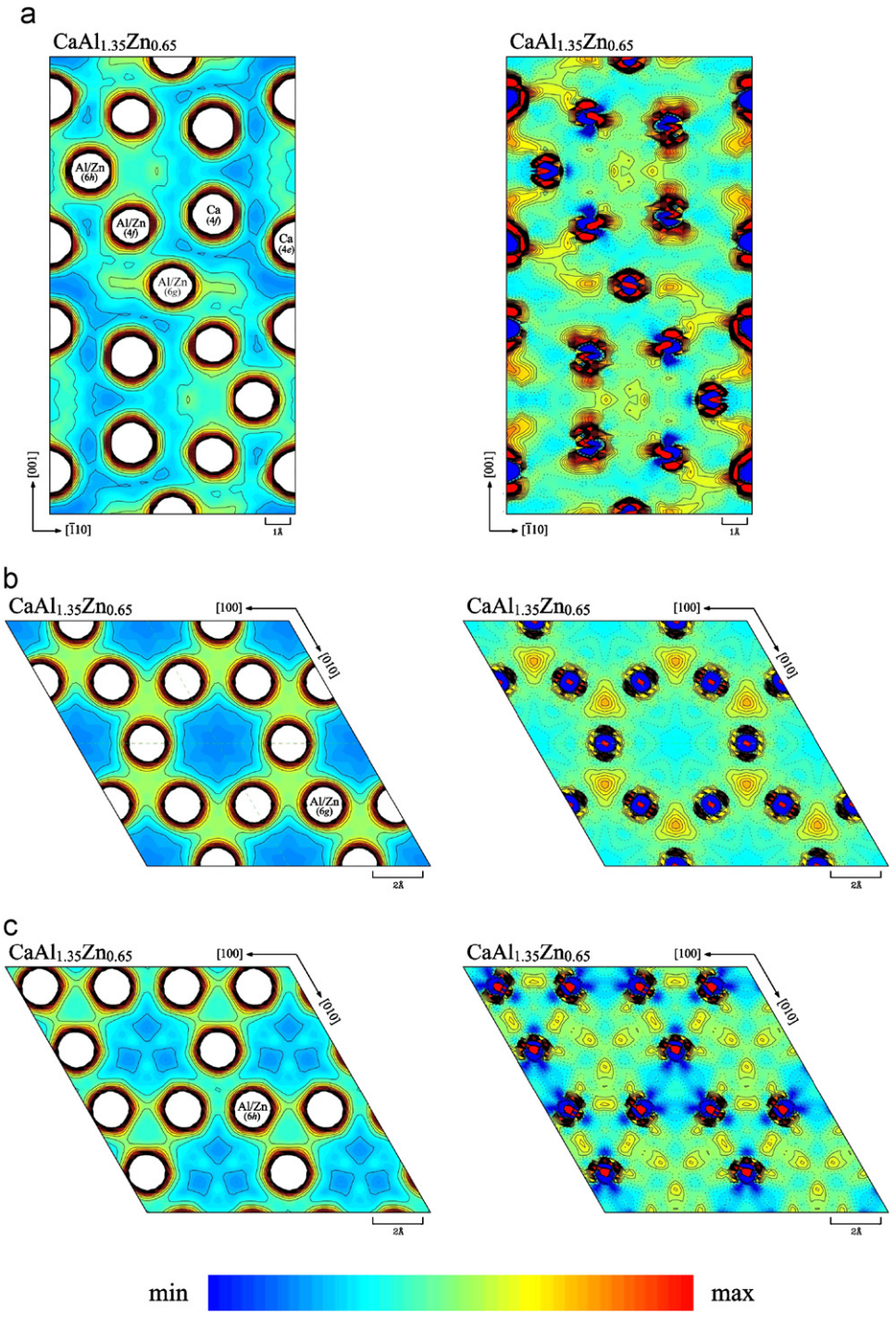

Fig. 7. The MEM charge (left) and the deformation charge (right) density maps of $CaAl_{1.35}Zn_{0.65}$. The (110) section (a), the (001) section at $z = 0$ (b), and the (001) section at $z = 1/4$ (c) are shown. The color code corresponds to a range (i) from 0.0 to 1.0 with a step of 0.05 e/Å^3 for the MEM map and (ii) from −0.2 to 0.2 with a step of 0.01 e/Å^3 for the deformation map.

For $CaAl_{1.7}Zn_{0.3}$, overlapping electron density and, correspondingly, maxima of the deformation density, can be found on the edges of the 6*g* Kagomé net and the edges of the capped triangles of the 6*h* Kagomé net, with the overlap being more pronounced in the 6*h* net. No significant overlap is observed between Ca and Al/Zn atoms or between Ca atoms.

In the case of $CaAl_{1.5}Zn_{0.5}$, the electron densities overlap significantly within the triangles of both the 6*g* and 6*h* Kagomé net. The two types of triangles in the 6*h* net differ by the magnitude of the overlap, being larger in the doubly capped triangles. Additional local maxima of deformation charge density are found inside $(Al,Zn)_3Ca$ tetrahedra where Al/Zn atoms occupy the 6*h* position.

In the 6*g* Kagomé net in $CaAl_{1.35}Zn_{0.65}$, overlapping electron density is observed in the centers of triangles, whereas in the 6*h* net, it is found on the edges of the doubly capped triangles. As for $CaAl_{1.5}Zn_{0.5}$, local deformation charge density maxima are observed in $(Al,Zn)_3Ca$ tetrahedra.

The different patterns of overlapping electron density within the 6*h* and 6*g* Kagomé nets may be influenced by the preferred occupation of the 6*h* sites with Zn. This possible influence can be qualitatively studied by comparing the calculated pseudo-electron density for models with the same composition, but with different arrangements of Zn atoms. Although the pseudo-electron density obtained from the electronic structure calculations may not capture all features visible in the all-electron density distribution obtained by MEM, we can observe different pseudo-electron density distributions near Zn–Zn and Zn–Al contacts for the two following structural models. In a model where two Zn atoms are placed on neighbouring 6*g* sites, the pseudo-electron density distribution remains fairly symmetric (i.e., it is very similar for the Zn–Zn and Zn–Al contacts) even though the sixfold symmetry of the Kagomé net is broken in this model. There is no increased overlap observed between the two Zn atoms. On the other hand, placing two Zn atoms on 6*h* sites leads to an increased overlap along the Zn–Zn contact and a slightly reduced Zn–Al overlap which can be interpreted as a more directional Zn–Zn bond compared to the 6*g* Kagomé net. Even though these observations are based on simplified models they suggest that replacing Al atoms with Zn on the 6*h* site has a larger influence on the electron density distribution than a substitution on the 6*g* site. The formation of Zn–Zn contacts on the 6*h* Kagomé net which is preferentially occupied by Zn atoms throughout the homogeneity range of the C36 phase may therefore contribute to the pronounced difference between the two Kagomé nets observed in the MEM electron density maps. However, this effect does not seem to depend strongly on the total Zn concentration or the VEC as similar electron distributions are observed for $x = 0.3$ and 0.65; The Zn-poor and the Zn-rich boundary of the stability range of the C36 phase.

4. Conclusion

Through analysis of synchrotron powder X-ray diffraction data by the MEM/Rietveld method, the electron density distributions were obtained for cubic and 4H hexagonal Laves phases in the system $CaAl_{2-x}Zn_x$. Overlapping electron densities, which play an important role in stabilizing the crystal structures, are clearly observed between *B* net atoms. Maxima in the deformation charge density maps are generally shifted off the direct *B*–*B* contacts in the Laves phases, indicating multi-center bonding.

The two different Kagomé nets in the C36 structure show distinct density distributions. Despite details of the density maps changing considerably with composition, the capped and uncapped triangles within the flexible Kagomé net can clearly be distinguished by considering the density in the net plane alone. On the other hand, the density distribution of the rigid Kagomé net is more homogeneous and resembles the distribution observed in the Kagomé net of cubic $CaAl_2$.

Besides the different patterns in the density maps, the two different Kagomé nets exhibit differences in composition: Zn atoms prefer the positions on the flexible Kagomé net, which is slightly distorted. Ab-initio total energy calculations on simplified ordered models of the C36 phase indicate both a tendency of preferential occupation of the flexible Kagomé net with Zn and its distortion.

The electron distribution around Ca atoms is close to spherical, although there is a little discernible deviation from spherical, and they are fairly isolated. These observations indicate that the *B* atoms are taking an essential role for formation of the structures and Ca atoms are located in the large cavities of the network formed by *B* atoms.

Acknowledgments

The authors thank Dr. M. Boström and Prof. Y. Grin for help with the sample preparation and scientific encouragement, Drs. Kenichi Kato and Keiichi Ohsaka, JASRI for technical supports in measurements at SPring-8, and Mr. Sam Stevens for proofreading the manuscript. This work has been partially supported by the Swedish Science Council, VR, and Japan Science and Technology Agency, JST. OT thanks Prof. K. Niizeki, Tohoku University, for discussion. The synchrotron radiation experiments were performed at SPring-8 BL02B2 with the approval of the Japan Synchrotron Radiation Research Institute (JASRI).

References

[1] J.B. Friauf, J. Am. Chem. Soc. 49 (1927) 3107.
[2] J.B. Friauf, Phys. Rev. 29 (1927) 34.
[3] F. Laves, Metallwirtschaft 14 (1935) 645.
[4] F. Laves, H. Witte, Metallwirtschaft 15 (1936) 840–842.
[5] F.C. Frank, J.S. Kasper, Acta Crystallogr. 11 (1958) 184–190;
F.C. Frank, J.S. Kasper, Acta Crystallogr. 12 (1959) 483–499, 12 (1959) 483–499.
[6] G. Nuspl, K. Polborn, J. Evers, G.A. Landrum, R. Hoffmann, Inorg. Chem. 35 (1996) 6922–6932.
[7] K. Söderberg, M. Boström, Y. Kubota, T. Nishimatsu, R. Niewa, U. Häussermann, Y. Grin, O. Terasaki, J. Solid State Chem. 179 (2006) 2690–2697.
[8] T. Ohba, Y. Kitano, Y. Komura, Acta Crystallogr. C 40 (1984) 1–5.
[9] Y. Kubota, M. Takata, M. Sakata, T. Ohba, K. Kifune, T. Tadaki, J. Phys. Condens. Matter 12 (2000) 1253–1259.
[10] Y. Kubota, M. Takata, M. Sakata, T. Ohba, K. Kifune, T. Tadaki, Jpn. J. Appl. Phys. 38 (Suppl. 38-1) (1999) 456–459.
[11] J. Hafner, J. Phys. F: Met. Phys. 15 (1985) 1879–1893.
[12] T. Yokosawa, K. Söderberg, M. Boström, D. Grüner, G. Kreiner, O. Terasaki, Z. Kristallogr. 221 (2006) 357–374.
[13] M. Takata, B. Umeda, E. Nishibori, M. Sakata, Y. Saito, M. Ohno, H. Shinohara, Nature 377 (1995) 46–49.
[14] M. Takata, N. Machida, E. Nishibori, B. Umeda, M. Sakata, K. Tanigaki, M. Kosaka, I. Hirosawa, J. Mizuki, Jpn. J. Appl. Phys. Suppl. 38-1 (1999) 122–125.
[15] S. Sasaki, Numerical tables of anomalous scattering factors calculated by the Cromer and Liberman's method, KEK Report 88-14, National Laboratory for High Energy Physics, Tsukuba, Japan, 1989.
[16] Y. Kubota, Program for Rietveld Analysis, rwpy917, 2005.
[17] H. Tanaka, M. Takata, E. Nishibori, K. Kato, T. Ishii, M. Sakata, J. Appl. Crystallogr. 35 (2002) 282–286.
[18] (a) G. Kresse, J. Hafner, Phys. Rev. B 47 (1993) 558;
(b) G. Kresse, J. Furthmüller, J. Phys. Rev. B 54 (1996) 11169.
[19] D. Vanderbilt, Phys. Rev. B 41 (1990) 7892.
[20] J.P. Perdew, A. Zunger, Phys. Rev. B 23 (1981) 5048.
[21] R.L. Johnston, R. Hoffmann, Z. Anorg. Allg. Chem. 616 (1992) 105–120.
[22] S. Amerioun, S.I. Simak, U. Häussermann, Inorg. Chem. 42 (2003) 1467–1474.